Commun. Comput. Phys.
doi: 10.4208/cicp.OA-2016-0109

Vol. **22**, No. 1, pp. 112-132
July 2017

Lagrangian Mesh Model with Regridding for Planar Poiseuille Flow

Jingxuan Zhuo[1], Ricardo Cortez[2] and Robert Dillon[1,*]

[1] *Department of Mathematics and Statistics, Washington State University, USA.*
[2] *Department of Mathematics, Tulane University, USA.*

Received 17 July 2016; Accepted (in revised version) 12 November 2016

Abstract. Many biological settings involve complex fluids that have non-Newtonian mechanical responses that arise from suspended microstructures. In contrast, Newtonian fluids are liquids or mixtures of a simple molecular structure that exhibit a linear relationship between the shear stress and the rate of deformation. In modeling complex fluids, the extra stress from the non-Newtonian contribution must be included in the governing equations.

In this study we compare Lagrangian mesh and Oldroyd-B formulations of fluid-structure interaction in an immersed boundary framework. The start-up phase of planar Poiseuille flow between two parallel plates is used as a test case for the fluid models. For Newtonian and Oldroyd-B fluids there exist analytical solutions which are used in the comparison of simulation and theoretical results. The Lagrangian mesh results are compared with Oldroyd-B using comparable parameters. A regridding algorithm is introduced for the Lagrangian mesh model. We show that the Lagrangian mesh model simulations with regridding produce results in close agreement with the Oldfoyd-B model.

AMS subject classifications: 74F10, 76Z05, 65M06, 92C10, 74S20, 74L15

Key words: Lagrangian mesh model, Oldroyd-B, immersed boundary method, viscoelastic fluid, regridding methods.

1 Introduction

Complex fluids have become a major focus of attention in fluid mechanics. Many biological fluids have suspended microstructures and may exhibit complex, non-Newtonian responses. These include mucus in the lung, as well as fluids in the stomach, intestines,

*Corresponding author. *Email addresses:* jxzhuo@hotmail.com (J. Zhuo), rcortez@tulane.edu (R. Cortez), dillon@math.wsu.edu (R. Dillon)

oviduct and uterus. A variety of analytical and numerical studies have emerged to investigate the mechanics of these fluids. The Oldroyd-B constitutive equations in an immersed boundary framework have been used to model complex fluids [5,8,12] and fluid-particle interactions [3, 10, 15, 20]. There are also several studies that use a Lagrangian mesh to model complex fluids [1,2,7,23,24].

An earlier numerical rheometer study [7] demonstrated that viscoelastic properties of an immersed boundary Lagrangian mesh model were very similar to those of an Oldroyd-B model [7]. Here we compare the two models in start-up Poiseuille flow. Planar Poiseuille flow between two parallel plates, also known as parabolic channel flow, driven by a constant spatially-uniform pressure gradient, is a well-known test problem for numerical algorithms. It is useful as a benchmark problem because of the existence of analytical solutions for both Newtonian and Oldroyd-B viscoelastic flow, thus allowing exact tracking of discretization and lagging-errors [9]. Waters and King (1970) studied the time-dependent start-up flow of viscoelastic fluids and found an analytical solution for planar Poiseuille flow. This solution can be compared with numerical simulation results using various model parameters, such as elasticity and Weissenberg number (W_i). The order of convergence of discretization errors can be established by successive refinement of the fluid grid, Lagrangian mesh. An important finding during the present course of study is that refinement of fluid grid or Lagrangian mesh, as well as remeshing of the Lagrangian mesh can produce velocity profiles that are very similar to the analytical solutions from the corresponding Oldroyd-B model.

2 Oldroyd-B model

The Oldroyd-B formulation [16] is frequently used to model complex fluids. Compared with Newtonian fluid, viscoelastic fluid can have a dilute suspension of high molecular weight polymer structures in a Newtonian solvent (water, glycerol, etc.). Distended polymers provide an extra stress to the solvent stress through random walks caused by collisions with solvent molecules. The Oldroyd-B (OB) model incorporates this additional stress by modeling this component separately and adding it to the total stress. An immersed boundary Oldroyd-B (IB-OB) method was proposed by [18] for Stokesian peristaltic pumping.

We shall consider the start-up flow of viscoelastic fluids in a planar channel. The flow is driven by an instantaneously applied uniformly distributed pressure gradient to the fluid initially at rest. The channel is bounded by two parallel plates with a separation distance $2H$. The channel flow has x-periodic geometry as illustrated in Fig. 1. An IB-OB model for 2D Poiseuille flow is formulated as follows. With the assumptions that the fluid is isothermal and incompressible, the fundamental conservation equations of linear momentum and mass within the fluid domain Ω are given by

$$\rho\left(\frac{D\mathbf{u}}{Dt}\right)=\nabla\cdot\mathbf{S}_{tot} \quad \text{and} \quad \nabla\cdot\mathbf{u}=0 \quad \text{in } \Omega, \tag{2.1}$$

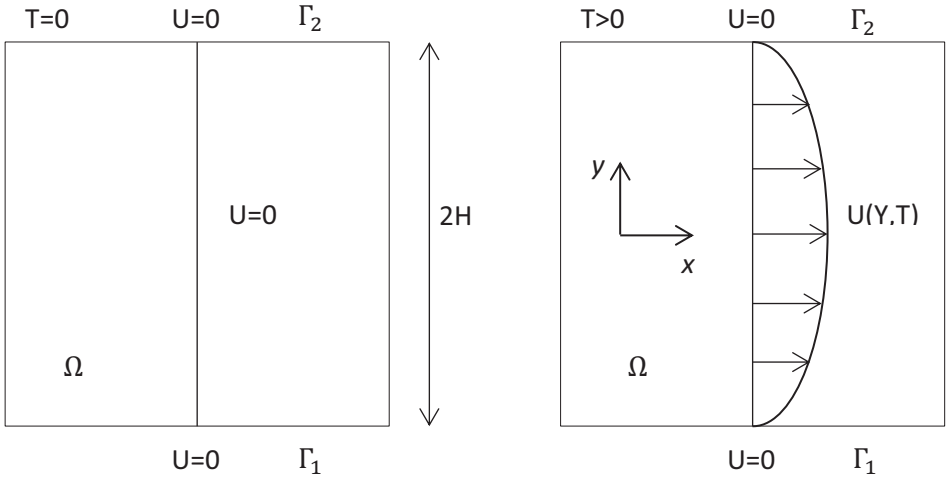

Figure 1: Schematic illustration of start-up planar Poiseuille flow.

with

$$\begin{aligned}&\mathbf{S}_{tot}=\mathbf{S}_s+\mathbf{S}_p,\\&\tau\mathbf{S}_p^{\nabla}=-(\mathbf{S}_p-G\mathbf{I})\quad \text{in }\Omega.\end{aligned}\tag{2.2}$$

Here $D/Dt=(\partial/\partial t)+\mathbf{u}\cdot\nabla$ is the material derivative, ρ is fluid density, $\mathbf{S}_{tot}$ is total stress tensor and is the sum of the Newtonian (solvent) stress tensor $\mathbf{S}_s$ and the polymer stress tensor $\mathbf{S}_p$ provided by polymer distensions [18]. The solvent stress tensor $\mathbf{S}_s=-p\mathbf{I}+2\mu\mathbf{E}$, where $\mathbf{E}$ is the rate of strain tensor $\mathbf{E}=(\mathbf{1/2})(\nabla\mathbf{u}+\nabla\mathbf{u}^{\mathbf{T}})$, p is pressure, and μ is the solvent viscosity. The polymer stress tensor $\mathbf{S}_p$ is unique to the complex flow of Oldroyd-B like fluids; it is zero for viscous fluids such as water and glycerol. τ is the time scale for polymer relaxation, and $G\mathbf{I}$ is the additional isotropic stress. The Oldroyd derivative (or upper-convected time derivative), $\mathbf{S}_p^{\nabla}$, is defined as

$$\mathbf{S}_p^{\nabla}=\frac{D\mathbf{S}_p}{Dt}-\nabla\mathbf{u}\cdot\mathbf{S}_p-\mathbf{S}_p\cdot\nabla\mathbf{u}^T.$$

After rearrangement, Eqs. (2.1) and (2.2) are transformed to

$$\rho\frac{D\mathbf{u}}{Dt}=-\nabla p+\mu\Delta\mathbf{u}+\nabla\cdot\mathbf{S}_p\quad\text{and}\quad\nabla\cdot\mathbf{u}=0\quad\text{in }\Omega,\tag{2.3}$$

$$\tau\left(\frac{D\mathbf{S}_p}{Dt}-\nabla\mathbf{u}\cdot\mathbf{S}_p-\mathbf{S}_p\cdot\nabla\mathbf{u}^T\right)=-(\mathbf{S}_p-G\mathbf{I})\quad\text{in }\Omega.\tag{2.4}$$

For parabolic channel flow we have $\mathbf{u}=0$ at the channel walls, Γ_1 and Γ_2. The channel walls are periodic in the x-direction. ρ, p, and μ are assumed to be constant. The time evolution Eq. (2.4) of $\mathbf{S}_p$ is coupled with the fluid momentum Eq. (2.3) to formulate the Oldroyd-B fluid model.

2.1 Analytical solutions

We consider the start-up flow of viscoelastic fluids in a planar channel bounded by two parallel plates as shown in Fig. 1. The flow is driven by a constant pressure gradient p' and enters a transient phase, where the velocity and stresses remain dependent upon time until an asymptotically steady state is reached.

Let $\mathbf{u}(x,y,t)$ be the fluid velocity vector with x-component u and y-component v. For fully developed 2-D Poiseuille flow, $v=0$ and $\nabla\cdot\mathbf{u}=\partial\mathbf{u}/\partial\mathbf{x}+\partial\mathbf{v}/\partial\mathbf{y}=\mathbf{0}$; hence Eq. (2.3) reduces to

$$\rho\frac{\partial u}{\partial t}=-\frac{\mathrm{d}p}{\mathrm{d}x}+\mu\frac{\partial^2 u}{\partial y^2}. \tag{2.5}$$

For fully developed viscoelastic fluid the extra-stress tensor $\mathbf{S}_p$ is added and the momentum equation is

$$\rho\frac{\partial u}{\partial t}=-\frac{\mathrm{d}p}{\mathrm{d}x}+\mu\frac{\partial^2 u}{\partial y^2}+\frac{\partial S_{12}}{\partial y}, \tag{2.6}$$

where S_{12} is the off-diagonal component of the polymer stress $\mathbf{S}_p$.

Analytical solutions to Eqs. (2.5) and (2.6) exist (see White [22] and Waters et al. [21]) for both Newtonian and viscoelastic Poiseuille flow (Oldroyd-B model). In the Newtonian case the analytical solution for start-up Poiseuille flow is given by [22]:

$$u(t,y)=-\frac{H^2p'}{2\mu}\left[\left(1-\frac{y^2}{H^2}\right)-32\sum_{n=1}^{\infty}\frac{\sin\left(\frac{\pi}{2}(2n-1)(1+\frac{y}{H})\right)\exp(-\frac{n^2\mu t}{4\rho H^2})}{(2n-1)^3\pi^3}\right]. \tag{2.7}$$

The fluid reaches the average steady-state velocity $\bar{u}_\infty=-H^2p'(x)/(3\mu)$ asymptotically as $t\to\infty$. Note that the fluid has spatial scale H and time scale $\rho H^2/\mu$.

For viscoelastic fluid the analytical solution is given by [21]:

$$u(t,y)=-\frac{H^2p'}{2\eta_0}\left[\left(1-\frac{y^2}{H^2}\right)-32\sum_{n=1}^{\infty}\frac{\sin\left(\frac{\pi}{2}(2n-1)(1+\frac{y}{H})\right)G_n(t)\exp(-\frac{\alpha_n t}{2\tau})}{(2n-1)^3\pi^3}\right], \tag{2.8}$$

where

$$G_n(t)=\begin{cases}\cosh(\frac{\beta_n t}{2\tau})+\frac{\gamma_n}{\beta_n}\sinh(\frac{\beta_n t}{2\tau}) & \text{if } \alpha_n^2\geq En^2,\\ \cos(\frac{\beta_n t}{2\tau})+\frac{\gamma_n}{\beta_n}\sin(\frac{\beta_n t}{2\tau}) & \text{if } \alpha_n^2<En^2.\end{cases} \tag{2.9}$$

and $\alpha_n=1+(1/4)\beta En^2$, $\beta_n=\sqrt{|\alpha_n^2-En^2|}$, $\gamma_n=1-(1/4)(2-\beta)En^2$. $\eta_0=\mu+\tau G$ is total zero-shear rate viscosity, and $\beta=\mu/\eta_0$ is the solvent viscosity ratio. E is the elasticity number defined by the ratio of Weissenberg (Wi) and Reynolds (Re) numbers:

$$Wi=\frac{\tau\tilde{u}_\infty}{H},\qquad Re=\frac{\rho H\tilde{u}_\infty}{\eta_0},\qquad E=\frac{Wi}{Re}=\frac{\tau\eta_0}{\rho H^2},$$

where the average steady-state velocity is $\tilde{u}_\infty=-H^2p'/(3\eta_0)$. The relaxation time of the viscoelastic fluid is τ.

2.2 Immersed boundary Oldroyd-B

The immersed boundary method, originally introduced by Peskin [17], has been used to capture coupled fluid-boundary structure interactions in viscoelastic fluid in many studies including [4, 8, 11, 19]. Here, the computational fluid domain is $4H\times 4H$. The top and bottom walls of the immersed boundary channel are placed at heights of $y=H$ and $y=3H$. Periodic boundary conditions are imposed on the fluid equations, with x-periodic conditions on the immersed boundary channel walls. Similar to the Stokes-OB model proposed by Teran et al. [18] the immersed-boundary Oldroyd-B model (IB-OB) governing equations are

$$\rho\frac{D\mathbf{u}}{Dt}=-\nabla p+\mu\Delta\mathbf{u}+\nabla\cdot\mathbf{S}_p+\mathbf{F}(\mathbf{x},t), \tag{2.10}$$

$$\nabla\cdot\mathbf{u}=0, \tag{2.11}$$

$$\tau\left(\frac{D\mathbf{S}_p}{Dt}-\nabla\mathbf{u}\cdot\mathbf{S}_p-\mathbf{S}_p\cdot\nabla\mathbf{u}^T\right)=-(\mathbf{S}_p-G\mathbf{I}), \tag{2.12}$$

$$\mathbf{F}(\mathbf{x},t)=\int_{\Gamma_{1,2}}\mathbf{f}(s,t)\delta_h(\mathbf{x}-\mathbf{X}(s,t))\mathrm{d}s, \tag{2.13}$$

$$\frac{\partial\mathbf{X}(s,t)}{\partial t}=\mathbf{u}(\mathbf{X}(s,t),t)=\int_{\Omega}\mathbf{u}(\mathbf{x})\delta_h(\mathbf{x}-\mathbf{X}(s,t))\mathrm{d}\mathbf{x}. \tag{2.14}$$

Here, $\mathbf{X}(s,t)$ is the Lagrangian description of the immersed boundary walls Γ_k, $k=1,2$, at time t. The Lagrangian force $\mathbf{f}(s,t)$ at $\mathbf{X}(s,t)$ is the elastic force per unit length along the walls due to the deformation. $\delta_h(\mathbf{x})$ is the 2-D Dirac delta function using Eulerian grid spacing h. $\mathbf{F}(\mathbf{x},t)$ is the Eulerian force per unit area exerted on the fluid domain Ω by the immersed boundaries.

In order to hold the channel walls at fixed positions, the wall Lagrangian force $\mathbf{f}$ is modeled with Hookean springs with zero rest lengths connecting the wall points $\mathbf{X}(s,t)$ to the fixed "tether" points $\mathbf{Z}(s)$, as shown below in Eq. (2.15) where the stiffness constant S is chosen as large as possible in order to tether the wall points to their initial positions.

$$\mathbf{f}(s,t)=S\big[\mathbf{Z}(s)-\mathbf{X}(s,t)\big]. \tag{2.15}$$

The system is closed in Eq. (2.14) by requiring that the elastic boundaries move at the local fluid velocity.

2.3 Numerical method

The 2D fluid domain is discretized using a uniform grid. Immersed boundaries, including boundary walls and other elastic structures, are modeled as curves which do not necessarily conform to the Eulerian fluid grid. The processes to convey momentum from boundaries to fluid and translate velocity from the Eulerian fluid grid to Lagrangian immersed boundaries are represented as two integrals: Eqs. (2.13)-(2.14). In the numerical

method we employ an approximate delta function as discussed in [6]: $\delta_h(\mathbf{x}) = d(x)d(y)$, where h is Eulerian grid spacing, and

$$d(x) = \begin{cases} \frac{1}{4h}\left(1+\cos\frac{\pi x}{2h}\right) & \text{if } \frac{|x|}{h} < 2, \\ 0 & \text{if } \frac{|x|}{h} \geqslant 2. \end{cases} \tag{2.16}$$

The Eulerian force density is obtained from the Lagrangian force density on the immersed boundary $\mathbf{X}$ at each time t:

$$\mathbf{F}_{ij} = \sum_m \mathbf{f}_m \delta_h(\mathbf{x}_{ij} - \mathbf{X}_m)\Delta s, \tag{2.17}$$

where Eq. (2.17) is a discretized version of Eq. (2.13), $\mathbf{f}_m$ is the Lagrangian force defined at each point $\mathbf{X}_m$ on the immersed boundaries Γ_k, $k=1,2$ and Γ_k is discretized as $\mathbf{X} = (\mathbf{X}_1, \mathbf{X}_2, \cdots, \mathbf{X}_p)$. The Eulerian fluid grid is denoted as $\mathbf{x}_{ij} = (ih, jh)$, $i=1,2,\cdots,n$, $j=1,2,\cdots,n$. $\mathbf{F}_{ij}$ is the Eulerian force applied on fluid per volume by the boundaries. Δs is the initial point separation along immersed boundaries Γ_k.

The fluid velocity of the m^{th} immersed boundary point is obtained via the following interpolation:

$$\mathbf{U}_m = \sum_{i,j} \mathbf{u}_{ij} \delta_h(\mathbf{x}_{ij} - \mathbf{X}_m) h^2 \tag{2.18}$$

which is a discretized version of Eq. (2.14), $\mathbf{u}_{ij}$ is the fluid velocity defined on the Eulerian fluid grid at $\mathbf{x}_{ij}$, $\mathbf{U}_m$ is the local Lagrangian velocity at the immersed boundary point $\mathbf{X}_m$. This expression uses δ_h to interpolate the Eulerian velocity to local Lagrangian structures. As the time step Δt is small (10^{-6}), Euler's method is used to update the immersed boundary configuration:

$$\mathbf{X}^{n+1} = \mathbf{X}^n + \Delta t \mathbf{U}^{n+1}. \tag{2.19}$$

Algorithm

The algorithm for solution of the IB-OB system can be summarized as follows. At the beginning of each time step n we have the discretized fluid velocity $\mathbf{u}^n$, immersed boundary points of the channel walls $\mathbf{X}^n$, and polymer stress $\mathbf{S}_p^n$. In order to update the system to time step $n+1$ we

1. Compute the Lagrangian force density $\mathbf{f}_m$ at each immersed boundary point.
2. Interpolate the forces to the Eulerian grid to obtain the force density $\mathbf{F}$.
3. Update the polymer stress to $\mathbf{S}_p^{n+1}$.
4. Solve the Navier-Stokes Eqs. (2.10)-(2.11) for $\mathbf{u}^{n+1}$.
5. Interpolate $\mathbf{u}^{n+1}$ to the immersed boundary points to obtain boundary velocities $\mathbf{U}^{n+1}$.
6. Update the boundary configurations $\mathbf{X}^{n+1}$.

We use a Fast Fourier Transform method for solving the Navier-Stokes Eqs. (2.10)-(2.11) [6]. Since the extra-stress matrix S_p is symmetric and $\mathbf{u}$ is incompressible, Eq. (2.12) can be represented by three equations:

$$\frac{\partial S_{11}}{\partial t}=2\left(\frac{\partial u}{\partial x}S_{11}+\frac{\partial u}{\partial y}S_{12}\right)-u\frac{\partial S_{11}}{\partial x}-v\frac{\partial S_{11}}{\partial y}-\frac{1}{\tau}(S_{11}-G), \tag{2.20}$$

$$\frac{\partial S_{12}}{\partial t}=\frac{\partial u}{\partial y}S_{22}+\frac{\partial v}{\partial x}S_{11}-u\frac{\partial S_{12}}{\partial x}-v\frac{\partial S_{12}}{\partial y}-\frac{1}{\tau}S_{12}, \tag{2.21}$$

$$\frac{\partial S_{22}}{\partial t}=2\left(\frac{\partial v}{\partial x}S_{12}+\frac{\partial v}{\partial y}S_{22}\right)-u\frac{\partial S_{22}}{\partial x}-v\frac{\partial S_{22}}{\partial y}-\frac{1}{\tau}(S_{22}-G). \tag{2.22}$$

We solve Eqs. (2.20)-(2.22) numerically using central differences for the spatial derivatives, upwind divided differences for the material derivative of $\mathbf{S}$ and a second-order Runga Kutta method for the time derivatives. In the application shown here we set $\mathbf{S}=G\mathbf{I}$ at time $t=0$.

3 Lagrangian mesh model

An immersed boundary Lagrangian mesh (IB-LM) method was introduced by Bottino [2] for modeling cellular actin cytoskeleton using a web of nodes that have viscoelastic linkages between the nodes. The initial location of nodes could be randomly chosen. Link connections could form and break, and could depend on the temporal history of the links. Bottino studied the macroscopic properties of the complex fluid as a property of these microscopic rules through several rheological experiments. A similar Lagrangian method has been used by [1] to study biofilm dynamics and by [7] in a computational rheometer.

We describe an IB-LM model for a viscoelastic fluid using a Lagrangian mesh consisting of a discrete set of immersed boundary mesh points $\mathbf{X}_m(t)$ initialized as a regular grid with equal grid spacing. In a 2D mesh, each immersed boundary node is connected to its 8 nearest neighbors in the vertical, horizontal and diagonal directions with viscoelastic links. The linkage can be modeled with Jeffreys or Maxwell elements or other types of linear elements as well as nonlinear viscoelastic links. The links used in this study are Maxwell elements. Since the nodes in the mesh move at the local fluid velocity, the mesh can become deformed over time introducing forces into the Navier-Stokes equations. The IB-LM equations are formulated as follows:

$$\rho\left(\frac{\partial \mathbf{u}}{\partial t}+(\mathbf{u}\cdot\nabla)\mathbf{u}\right)=-\nabla p+\mu\Delta\mathbf{u}+\mathbf{F}_e+\mathbf{F}_m, \tag{3.1}$$

$$\nabla\cdot\mathbf{u}=0, \tag{3.2}$$

$$\frac{\partial \mathbf{X_i}}{\partial t}=\mathbf{u}(\mathbf{X_i}(s,t),t)=\int\mathbf{u}(\mathbf{x},t)\delta(\mathbf{x}-\mathbf{X_i}(s,t))d\mathbf{x} \tag{3.3}$$

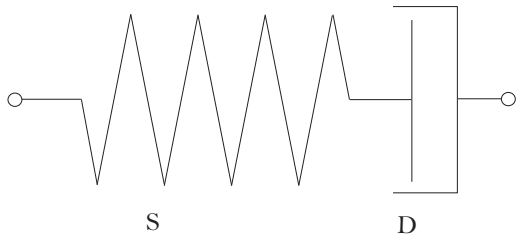

Figure 2: Maxwell element.

and

$$\mathbf{F_i}(\mathbf{x},t)=\int_\Gamma \mathbf{f_i}(s,t)\delta(\mathbf{x}-\mathbf{X_i}(s,t))ds, \tag{3.4}$$

where $i=e$ is the immersed boundary elastic structure and $i=m$, the immersed boundary Lagrangian viscoelastic mesh.

Each Maxwell element, as shown in Fig. 2, consists of a dashpot D and a spring S connected in series. If we let x be the total length of the element, then

$$x=x_1+x_2+L, \tag{3.5}$$

where x_1 is the spring extension from its resting length L, and x_2 is the creep length in the dashpot D. In the Maxwell element, the spring force is equal to the dashpot force,

$$\kappa x_1=\nu\dot{x}_2, \tag{3.6}$$

where κ is the spring stiffness and ν the dashpot viscosity. With $\dot{x}=\dot{x}_1+\dot{x}_2$, this can be expressed as a first order ordinary differential equation for x_1

$$\dot{x}_1+\frac{1}{\lambda}x_1=\dot{x}, \tag{3.7}$$

where $\lambda=\nu/\kappa$ is the relaxation time for the stress generated by a strain to dissipate.

The solution for x_1 is given by

$$x_1(t)=e^{-(t-t_0)/\lambda}x_1(t_0)+\int_{t_0}^{t}\dot{x}(\tau)e^{-(t-\tau)/\lambda}d\tau \tag{3.8}$$

or equivalently

$$\sigma(t)=e^{-(t-t_0)/\lambda}\sigma(t_0)+\kappa\int_{t_0}^{t}\dot{x}(\tau)e^{-(t-\tau)/\lambda}d\tau \tag{3.9}$$

for the stress $\sigma(t)=\kappa x_1$.

In the Lagrangian mesh model, force is interpreted as force per unit length. At each of the Lagrangian mesh points, we use Eq. (3.9) above to compute the force due to each Maxwell element. The force at each of the mesh points is spread to the Eulerian grid via Eq. (3.4).

A formal relationship between the IB-OB and IB-LM methods was derived by [7]. Using the relationship that the Maxwell element relaxation time $\lambda=\nu/\kappa$ is the ratio of dashpot viscosity ν and spring stiffness κ, Eq. (3.7) can be expressed as $\lambda\dot{\sigma}+\sigma=\nu\dot{x}$ and generalized to the upper convected Maxwell model [13] for the Maxwell stress tensor $\mathbf{\Sigma}$

$$\lambda\left(\frac{D\mathbf{\Sigma}}{Dt}-(\nabla\mathbf{u}\cdot\mathbf{\Sigma}+\mathbf{\Sigma}\cdot\nabla\mathbf{u}^T)\right)+\mathbf{\Sigma}=2\nu\mathbf{D}, \tag{3.10}$$

where $\mathbf{D}=(1/2)(\nabla\mathbf{u}+\nabla\mathbf{u}^T)$. Let $\mathbf{\Sigma}=\mathbf{S}_p-G\mathbf{I}$, where $G\mathbf{I}$ is the additional isotropic stress in a complex fluid arising from thermodynamic fluctuations of the polymer chains [14], and setting $\lambda=\tau$ and $\lambda G=\nu$, Eq. (3.10) becomes formally equivalent to Eq. (2.4). The equivalence is achieved by setting the Maxwell element relaxation time λ equal to the OB fluid polymer relaxation time scale τ, and spring stiffness κ equal to the additional isotropic stress G in the OB fluid.

3.1 Lagrangian mesh regridding

The Lagrangian mesh is initialized as a uniform mesh grid. When the fluid is driven by a pressure gradient, as in the case of Poiseuille flow, the mesh moves with the local fluid velocity. The Lagrangian mesh experiences a deformation as the mesh nodes move away from the original uniform configuration. The deformation can lead to significant elongation and compaction of the individual mesh elements. In planar Poiseuille flow the fluid velocity reaches a maximum along the centerline of the fluid domain and gradually decreases from the centerline to the boundaries where the velocity is zero, forming a parabolic velocity profile. Mesh nodes near the centerline therefore move at much faster rates than nodes further away from the centerline. Because of this velocity differential, the nodes near the walls lag behind the centerline nodes over time.

A regridding step can be employed to solve this problem, remove the lagging effects caused by velocity differentials, improve the Lagrangian mesh model, and add to algorithm stability. The extra stress contribution to the viscoelastic fluid is modeled using the Lagrangian mesh. As the mesh is restored to a uniform grid, link forces on the deformed mesh are interpolated to nodes on the uniform mesh. The restored mesh is a regular grid and the target link force vectors are along the divisions of the octants. The regridding procedure is performed on each mesh node, and for each node loops through all eight link forces. First, each link force is decomposed along the division boundary directions of the octant in which the force resides (see Fig. 3). Second, the component forces are then interpolated to nearby nodes on the mesh. In this study, we use a 2-by-2 interpolation range so that the forces are distributed to the four vertices of the square that includes the node currently in focus.

Given the forces $\vec{\sigma}_k$ for $k=1,2,\cdots,8$ at locations $\vec{x}_j$ (Fig. 3a), which do not in general coincide with a uniform grid due to the Lagrangian motion, the goal is to interpolate the forces onto new locations corresponding to nodes on a uniform grid along the 8 directions $m\pi/4$ for $m=1$–8.

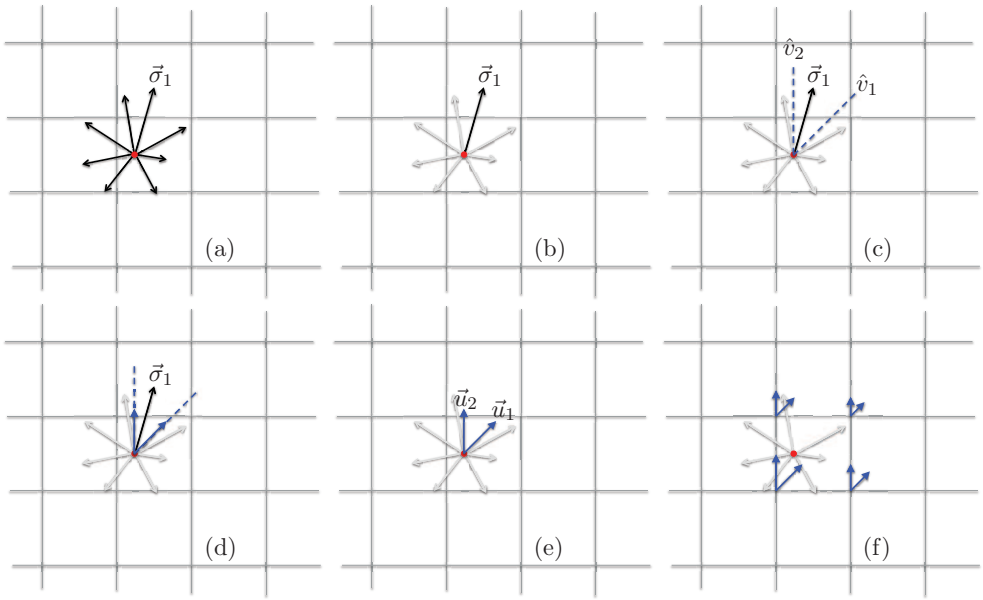

Figure 3: Regridding procedure.

1. Starting with $\vec{\sigma}_1$ in Fig. 3b, find the octant where it lies (Fig. 3c).
2. Using the two unit vectors $\hat{v}_1$ and $\hat{v}_2$ for that octant as a basis for $\mathbb{R}^2$, Fig. 3c, decompose $\vec{\sigma}_1$ into $\vec{\sigma}_1 = \vec{u}_1 + \vec{u}_2$ (Fig. 3d).
3. Interpolate the new force vectors $\vec{u}_1$ and $\vec{u}_2$ in Fig. 3e to the nearby nodes of the uniform grid (Fig. 3f). This procedure is repeated for each of the eight vectors at each node; then it is done for all the Lagrangian mesh nodes.

3.2 IB-LM Algorithm

At the beginning of each time step t^n, we have the immersed boundary configurations $\mathbf{X}_i^n$, for $i = e,m$ and fluid velocities $\mathbf{u}^n$. In order to update the fluid velocities and the immersed boundaries at time t^{n+1} we:

1. Calculate the force $\mathbf{f}_e^n$ using the immersed boundary configuration $\mathbf{X}_e^n$.
2. Calculate the Lagrangian mesh link forces using Eq. (3.9) from the Lagrangian mesh configuration $\mathbf{X}_m^n$ to produce the mesh force $\mathbf{f}_m^n$.
3. Interpolate the force densities $\mathbf{f}_i^n$ using Eq. (3.4) to the Eulerian grid to obtain $\mathbf{F}_i^n$.
4. Restore Lagrangian mesh forces to a uniform mesh using regridding every M time steps.
5. Solve Eqs. (3.1) and (3.2) to obtain $\mathbf{u}^{n+1}$.
6. Advect the immersed boundary points using Eq. (3.3) to obtain $\mathbf{X}_i^{n+1}$.

4 Results

In this section the numerical methods outlined in Sections 2.2 and 3.2 are applied to the 2-D Poiseuille flow problem. For the IB-OB and Newtonian models, analytical fluid velocity profiles at various times are compared with simulation results. Velocity profiles from IB-LM simulations are then compared with IB-OB results showing the difference between results over time. The following simulations are carried out with parameter values shown in Table 1.

Table 1: 2-D Poiseuille flow properties.

Parameter	Symbol	Units	Value
Time step	Δt	s	1.0×10^{-6}
Tether constant	k	g/s^2	8.0×10^{8}
Density	ρ	g/cm^3	1.0
Viscosity	μ	$g/(cm\ s)$	0.01
Pressure gradient	p'	$g/(cm^2\ s^2)$	-1000
Reynolds number	Re	–	0.1389
Viscosity ratio	β	–	1/9
Domain size	$4H$	cm	0.06
Weissenberg number.	W_i	–	0.1389
Spring stiffness	κ	$g/(cm\ s^2)$	32
Dashpot viscosity	ν	$g/(cm\ s)$	0.08
Regridding frequency	M	time step	100

The analytical solutions provide a reference for comparison with numerical simulations by keeping track of discretization errors over time with various spatial and time discretizations, making possible the comparison of convergence rates across various discretization and regridding schemes, using different flow parameters (e.g. β) and numerical methods. To facilitate the comparisons, we use nondimensional spatial scale $Y=y/H$; dimensionless time $T=\mu t/(\rho H^2)$ in the Newtonian case, $T=t/\tau$ in IB-OB with $\tau=\nu/\kappa$ in IB-LM; and dimensionless velocity $U=u/\bar{u}_\infty$ for Newtonian and $U=u/\tilde{u}_\infty$ for IB-OB and IB-LM.

In the case of Poiseuille flow, we define the $E(T)$ as the discretization error of a velocity profile at a fixed laboratory frame $x=\hat{X}$ at a given time T as the mean square of the difference of computational and analytical solutions:

$$E(T)=\sqrt{\frac{1}{n}\sum_{i=1}^{n}[\hat{U}(\hat{X},Y_i,T)-U(Y_i,T)]^2}, \tag{4.1}$$

where $\hat{U}(\hat{X},Y_i,T)$ is numerical grid velocity at $\hat{X}$ for Y_i, i=1,2,$\cdots$,n with fluid grid spacing $2H/n$ and dimensionless time T. $U(Y_i,T)$ is the corresponding analytical solution. The

relative discretization error

$$\tilde{e}(T) = \sqrt{\frac{\sum_{i=1}^{n} [\hat{U}(\hat{X}, Y_i, T) - U(Y_i, T)]^2}{\sum_{i=1}^{n} U(Y_i, T)^2}} \tag{4.2}$$

expresses the discretization error of simulation results relative to the analytical solution at each time T.

Newtonian Poiseuille flow exhibits a monotonically accelerating phase during start-up. Fig. 4 depicts the dimensionless centerline velocity profile at a fixed point over time. Initially the centerline velocity accelerates rapidly. This acceleration gradually slows as the centerline velocity approaches an asymptotic steady velocity. During the initial start-up period, the fluid velocity increases monotonically. The velocity toward the center of the channel is always greater than that further away from the centerline, with the maximum speed achieved at the center. As shown in Fig. 4, the Newtonian numerical simulations closely match the analytical solution.

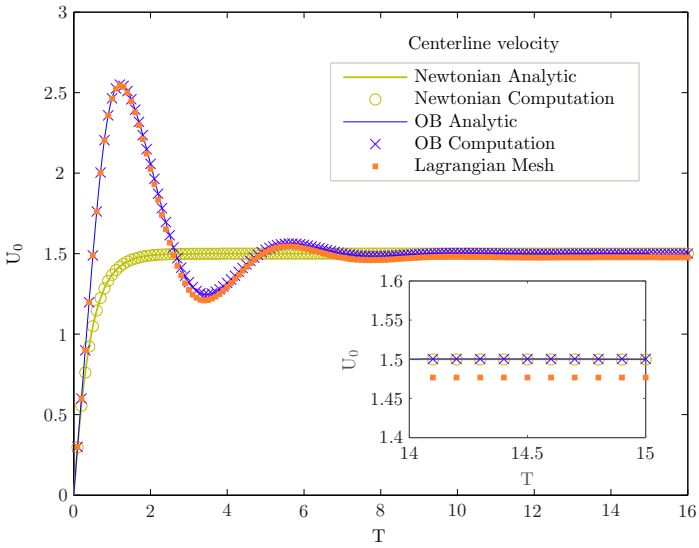

Figure 4: Centerline velocity of Newtonian, OB analytical, IB-OB simulation and IB-LM model; inset: magnified view on $T \in [14,15]$.

Viscoelastic flow also has a rapid acceleration in the initial period before approaching an asymptotic steady state which is at the same velocity as that of Newtonian fluid. Viscoelastic fluid, however, sees noticeable variations in the start-up phase. As in the case of Newtonian flow, IB-OB flow experiences a rapid rise in velocity, but attains a much higher speed than Newtonian flow and overshoots the steady state. Subsequently, the centerline velocity approaches the asymptotic steady state velocity in an oscillatory manner. The

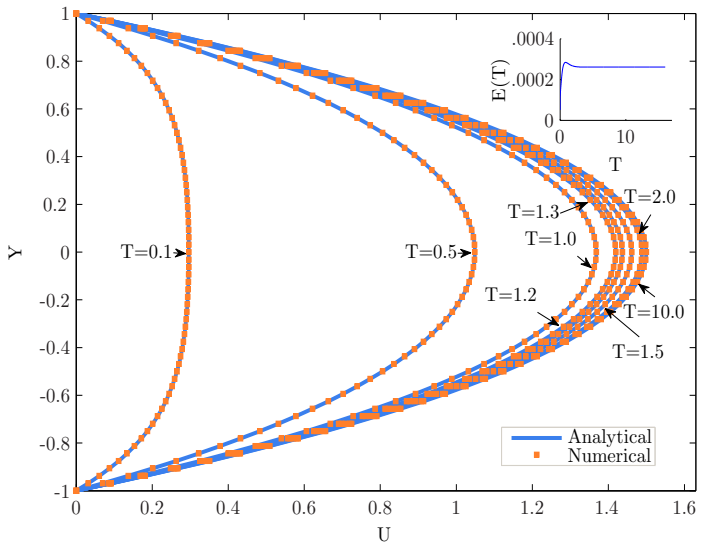

Figure 5: Newtonian Poiseuille flow analytical and computational velocity profiles; inset: discretization error for Newtonian fluid simulation.

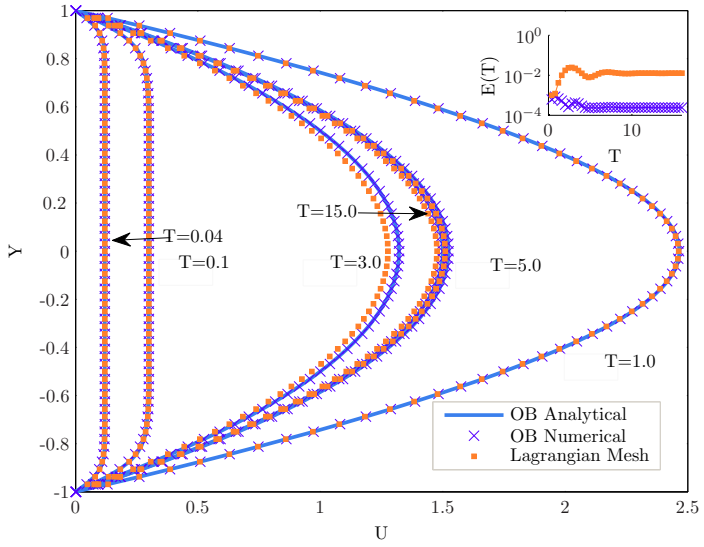

Figure 6: Viscoelastic flow analytical (IB-OB) and computational (IB-OB, IB-LM) velocity profiles; inset: discretization error for viscoelastic simulations.

numerical results and analytical solutions in OB flow are very similar. IB-LM Poiseuille start-up flow results are also very similar to IB-OB. Figs. 5 and 6 show analytical and numerical velocity profiles at several different times during the start-up phase of Newtonian, IB-OB, and IB-LM simulations. Taken at a fixed position in a laboratory frame, these

velocity profiles record the changes of velocity in this transient process. While Newtonian and IB-OB simulations show dissimilar profiles during the transient startup phase, the steady state profiles are very similar. The OB fluid experiences a much longer (5 times as long in the simulations shown) transient period before converging to a steady state. Consistent with the centerline velocity picture, OB fluid velocity profiles shown in Fig. 6 show a rapid overshoot at the beginning ($T=1.0$). The velocity profile drop below the steady velocity ($T=3.0$), then move ahead at ($T=5.0$). The centerline velocity shows a diminishing oscillatory form before finally reaching an approximate asymptotic steady state shown at ($T=15$).

4.1 IB-LM with regridding

The location of each node in the mesh is updated at every time step moving at the local fluid velocity. Over time the mesh shows a significant deformation from its initial configuration. In 2-D planar Poiseuille flow, the deformation can lead to a significantly lower steady state velocity levels relative to the OB analytical result. To overcome this difficulty, a regridding procedure is applied at regular time intervals. This improves stability and leads to results close to the IB-OB model.

Fig. 7 shows the velocity profiles obtained at different remeshing frequencies in IB-LM simulations. Consistent with Fig. 6, IB-OB simulation velocity profiles overlap with analytic predictions in both the initial start-up phrase and as they approach the stable state. However, velocity profiles from the IB-LM simulations show a discrepancy from the analytic OB solution. This discrepancy grows as the remeshing interval increases. Fig. 7 shows IB-LM velocity profiles at different times under different remeshing intervals.

In Fig. 7 (a-d), remeshing intervals vary from 5000 to 30000. At $T=1$ the velocity profiles of the viscoelastic analytic solution, as well as the IB-OB and IB-LM simulations are nearly identical. As already noted, the centerline velocity profiles (see Fig. 8) of the analytic solution have an initial excursion that greatly exceeds the asymptotic steady state centerline velocity and exhibits a transient oscillation as the centerline velocity approaches the steady state velocity. The IB-OB simulation results are in close agreement with the analytical solutions as seen in the centerline velocities shown in Fig. 8 as well as in the velocity profiles shown in Fig. 7. The discrepancy between the IB-LM simulations and the analytical results depends rather dramatically on the remeshing frequency. At a remeshing frequency of 10 the IB-LM centerline velocity as well as the velocity profiles are in close agreement with the analytical and IB-OB results. As seen in Figs. 7(a) and 8, when the remeshing is much less frequent, velocities significantly lag the IB-OB and analytical velocities at $T=3$, and continue to lag the IB-OB and analytical results at $T=15$. Moreover, as the remeshing interval increases, the discrepancies between the IB-LM and IB-OB/analytical solutions increase.

A similar "lagging" effect is seen in IB-LM velocities as shown in Fig. 7d: while the IB-LM velocity is close to the IB-OB and analytical results in the initial period ($T=1.0$), the IB-LM velocity gradually slows and lags behind the IB-OB/analytical profiles at later

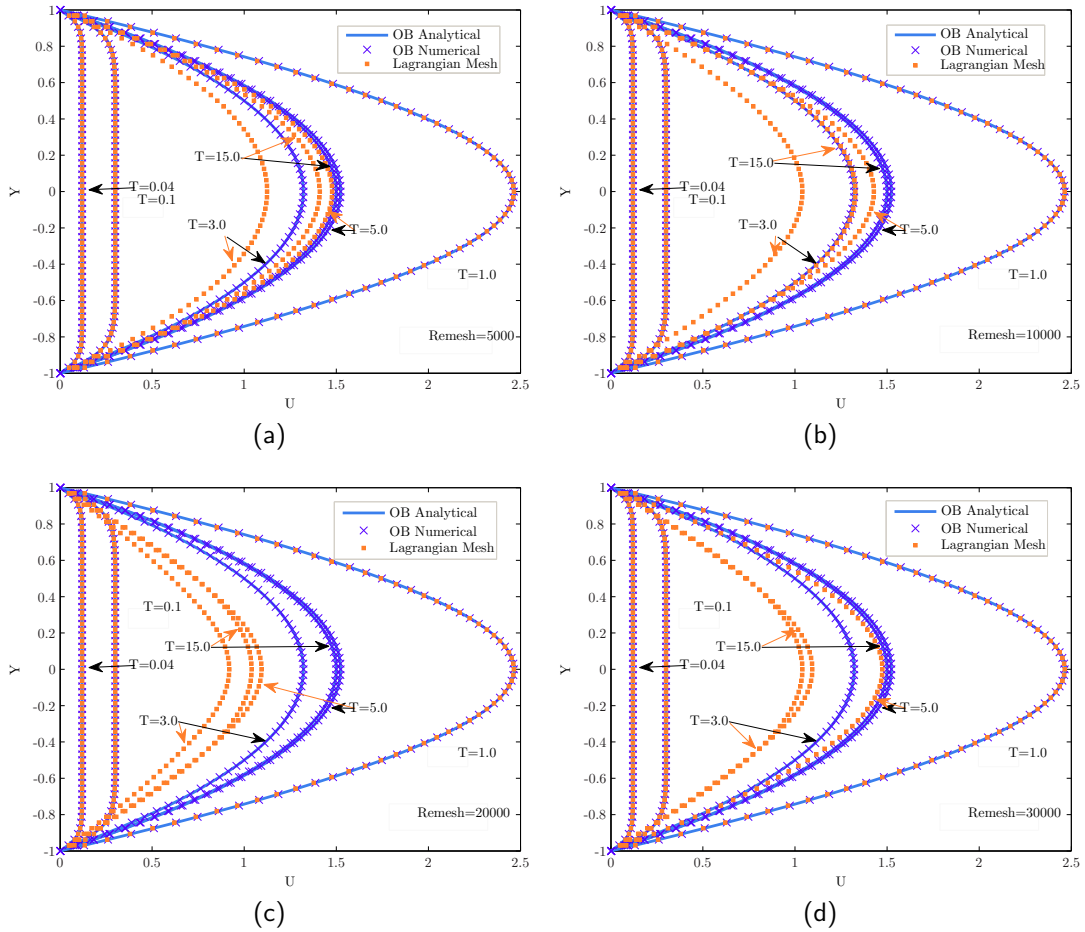

Figure 7: Velocity profiles at different remeshing frequencies.

times ($T=3.0,5.0,15.0$). As the remeshing interval becomes large, IB-LM velocities drop to even lower levels at later times. This effect is also seen in the centerline velocities shown in Fig. 8. Before $T=2.5$ there is no significant departure from the IB-OB results, but after the first velocity peak, IB-LM centerline velocity differences emerge, becoming larger with longer remeshing intervals. With remeshing intervals from 10 to 30000, IB-LM centerline velocity drops to the lowest level over time at the longest remeshing interval 30000. Centerline velocities at a remeshing interval of 10 exhibit much better agreement with its IB-OB counterpart. Centerline velocities at other remeshing intervals between 10 and 30000 show a "best fit" at 10 and worst at 30000. At less frequent remeshing the centerline velocity of the fluid still mimics the crest and trough characteristics of the start-up period in OB but at a lower magnitude; without remeshing IB-LM fluid undergoes similar velocity oscillations before approaching a steady state. After each remeshing step, fluid velocities quickly move towards the OB results, forming a peak which tends to rise

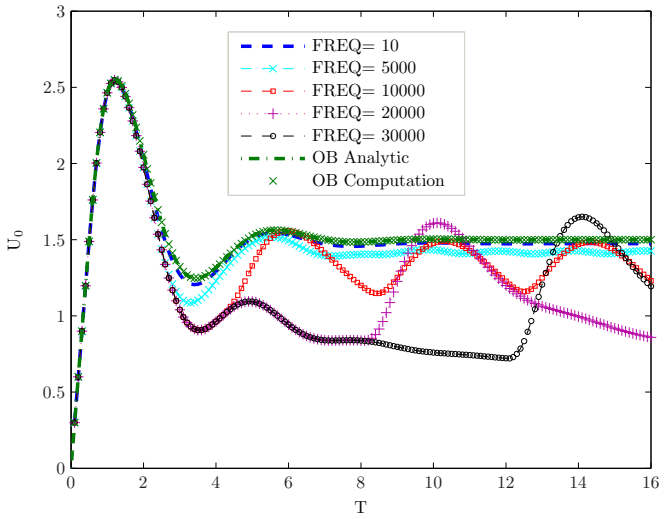

Figure 8: Centerline velocity over time at different remeshing schemes for model: fluid grid: 128-by-128, mesh grid: 64-by-64.

to or above the OB steady level. The peak then falls below the steady level and reaches its minimum level at the next remeshing point and then rises again to the next peak (see Fig. 8). For less frequent remeshing, centerline velocities drop lower and bounce to a higher level after each remeshing step. At remeshing intervals of 20000 and 30000, the velocity rises above the OB level before decreasing.

Figs. 9 and 10 show the relative discretization error in comparison with the analytic solutions over time for remeshing intervals of 5-1250 (Fig. 10) and 1250-30000 (Fig. 9). Included in each figure is the relative discretization error of the OB solution in comparison with the analytical results. These results show that there is a relative discretization error of approximately 10^{-3} for the IB-OB solutions and a larger error of 10^{-2} in IB-LM simulations with frequent remeshing. Moreover, the relative discretization errors are much larger with less frequent remeshing. As shown in Fig. 10 and highlighted in the figure inset, the differences between remeshing intervals of 5, 250, 500 are modest.

As regridding become more frequent, relative discretization errors between IB-LM results and the OB analytical solutions decrease. Less frequent remeshing, shown in Fig. 9, exhibits a greater deviation from the analytical result than more frequent remeshing, shown in Fig. 10. This effectively shows the result of remeshing: soon after mesh regridding, the discretization errors significantly decrease. As the effect of remeshing dissipates, discretization errors again rise until the next remeshing is applied, forming a series of peaks and valleys. The centerline velocity exhibits an oscillatory pattern with decreasing amplitudes, consistent with the characteristic of complex parabolic flow which converge to a steady velocity after an initial start-up phase. Like the OB fluid, IB-LM model at less frequent remeshing intervals eventually approaches a steady state at remeshing intervals of 20000 and 30000 steps.

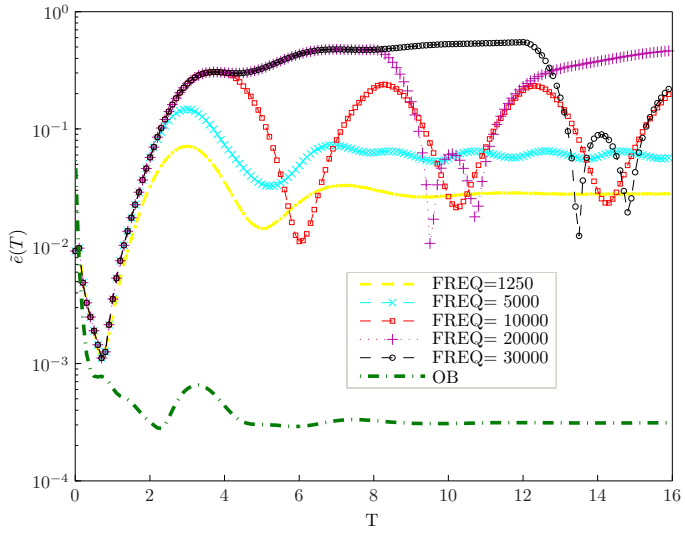

Figure 9: Relative discretization error at lower remeshing frequencies (interval beyond 1250).

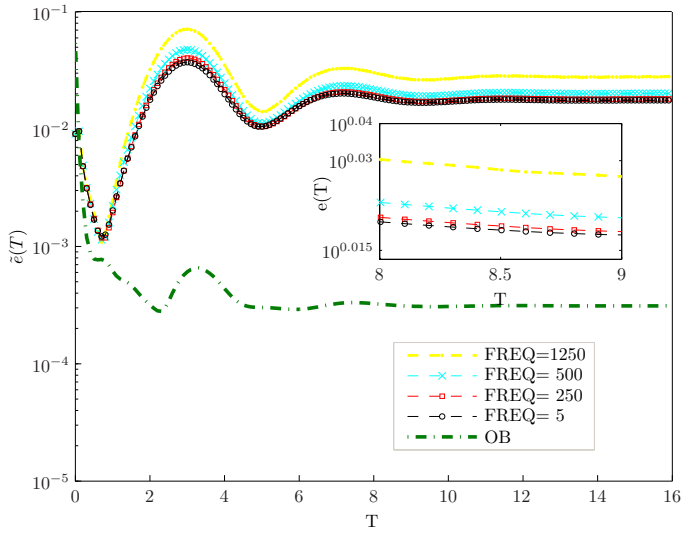

Figure 10: Relative discretization error at higher remeshing schemes (interval below 1250). Inset: magnified view on $T \in [8,9]$.

As shown in Fig. 11, more frequent remeshing reduces the discretization error and increases the computational cost as measured in CPU time. With the fluid and mesh grids shown here, the discretization error curve is rather flat until a regridding frequency of about 500. Conversely, the computational cost or regridding is negligible until a regridding frequency of about 50. Thus, a regridding every 50 to 500 time steps produces low discretization errors with a minimal computational cost.

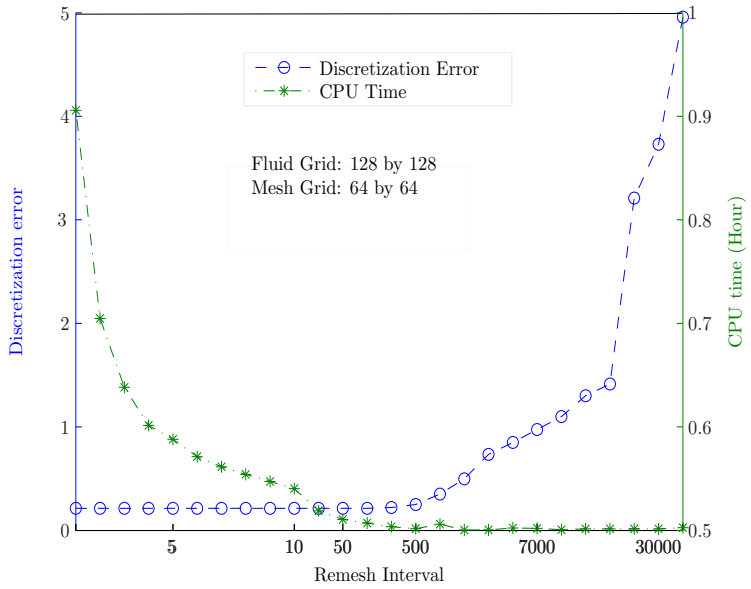

Figure 11: Discretization error and CPU time at various remeshing frequencies: fluid grid: 128-by-128, mesh grid: 64-by-64.

4.2 Refining the IB-LM mesh

In addition to regridding the Lagrangian mesh at regular time intervals, refinement of the Lagrangian mesh is shown to reduce the discretization errors in the IB-LM simulations. Fluid grids of 64-by-64, 128-by-128 and 256-by-256 were tested, and for each of these grid spacings, 7 different Lagrangian mesh grid spacings were considered. CPU-time and discretization errors are shown in Fig. 12,where the grid ratio is the ratio of fluid grid to mesh grid, and the error ratio is the ratio of discretization error relative to that of the finest grid. Similarly, the CPU-time ratio is relative to the base model consuming the least amount of CPU time. Both ratios start from 1. The simulations with a 256-by-256 fluid grid shows the lowest relative discretization errors. On the 256-by-256 fluid grid the discretization error ratios are most consistent over different grid ratios. At fluid grids of 64-by-64 and 128-by-128, the discretization error ratios show dramatic upturns as the grid ratio increases. While at the fluid grid of 256-by-256, the error ratio remains near 1. As the Lagrangian mesh grid becomes less coarse, the 256-by-256 fluid grid results show the least increase in the CPU time ratio, while the CPU time ratio rises above 20 as the mesh grid becomes more dense for 128-by-128 and 64-by-6 simulations. In terms of relative discretization error, the 256-by-256 fluid grid with 256-by-256 mesh grid is closer to OB than all the others. The 256-by-256 fluid grid with 128-by-128 mesh grid simulation shows a high degree of agreement the simulation with 128-by-128 fluid grid and 64-by-64 mesh grid.

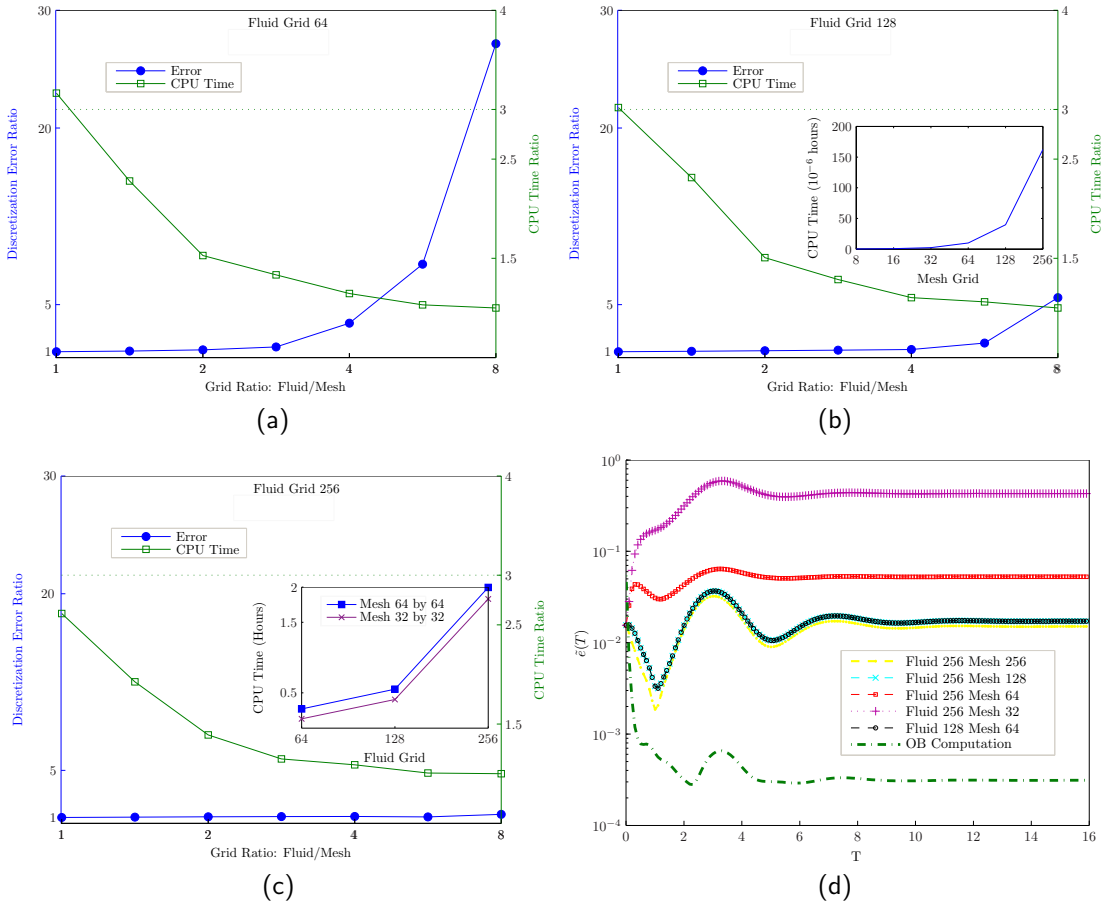

Figure 12: (a)∼(c): Discretization error and CPU time at different fluid and mesh gridding schemes; (d): relative discretization error at different gridding schemes.

5 Discussion

In this study we developed a Lagrangian mesh model in an immersed boundary framework using 2D planar Poiseuille flow as a test case. The Lagrangian mesh used in this study is initialized as a regular mesh grid using linear Maxwell connecting elements. In an earlier numerical rheometer study [7], this form of the Lagrangian mesh model gave very similar results to an Oldroyd-B model with comparable parameters. Here we compared the two models (IB-LM and IB-OB) in planar Poiseuille flow in terms of centerline speed, fixed frame velocity profile and discretization error, and we found remeshing, as well as fluid and/or mesh refinement increase the stability and accuracy of Lagrangian mesh simulations and produce results highly comparable with that of the Oldroyd-B model. We showed that the two models gave closer results as the fluid and mesh grid was refined.

This study explored the trade-offs between discretization error and CPU time consumption at various regridding frequencies, and determined an optimal regridding interval. Fixing the regridding scheme, this study then explored the same trade-offs of different fluid and mesh gridding schemes and found the optimal scheme.

Here we focused on planar Poiseuille flow with a low Reynolds number and a fixed set of parameters including the Weissenberg number W_i and the viscosity ratio β. In principle, Lagrangian mesh models can be used to model a variety of viscoelastic fluids. The form of the mesh could be regarded as a coarse grain model of the physical structure of the viscoelastic component of the fluid and, in some contexts, distortion of the mesh may have a physical interpretation and regridding would be unnecessary. Future investigations will examine alternative models for the viscoelastic links and comparisons with properties of viscoelastic media such as mucus, biological tissues, and biofilms.

Acknowledgments

We would like to thank Isaac Klapper for many helpful discussions about Lagrangian mesh rheometry. Z. Zhuo was supported in part by NSF grant DMS-0652535; R. Dillon was supported in part by NSF grants DMS-0652535 and DMS-1317671.

References

[1] ALPKVIST, E., AND KLAPPER, I. Description of mechanical response including detachment using a novel particle method of biofilm/flow interaction. *Wat. Sci. Tech. 55* (2007), 265–273.

[2] BOTTINO, D. C. Modeling viscoelastic networks and cell deformation in the context of the immersed boundary method. *J. Comput. Phys. 147* (1998), 86–113.

[3] CHRISPELL, J., AND FAUCI, L. Peristaltic pumping of solid particles immersed in a viscoelastic fluid. *Mathematical Modelling of Natural Phenomena 6* (2011), 67–83.

[4] CHRISPELL, J. C., CORTEZ, R., KHISMATULLIN, D. B., AND FAUCI, L. J. Shape oscillations of a droplet in an oldroyd-b fluid. *Physica D: Nonlinear Phenomena 240*, 20 (2011), 1593 – 1601. Special Issue: Fluid Dynamics: From Theory to Experiment.

[5] DASGUPTA, M., LIU, B., FU, H. C., BERHANU, M., BREUER, K. S., POWERS, T. R., AND KUDROLLI, A. Speed of a swimming sheet in newtonian and viscoelastic fluids. *Phys. Rev. E 87* (Jan 2013), 013015.

[6] DILLON, R., AND OTHMER, H. G. A mathematical model for outgrowth and spatial patterning of the vertebrate limb bud. *J. Theor. Biol. 197*, 3 (1999), 295 – 330.

[7] DILLON, R., AND ZHUO, J. Using the immersed boundary method to model complex fluidsstructure interaction in sperm motility. *DCDS-Series B 15*, 2 (2011), 343–355.

[8] DU, J., GUY, R. D., AND FOGELSON, A. L. An immersed boundary method for two-fluid mixtures. *J. Comput. Phys. 262* (2014), 231–243.

[9] DUARTE, A. S. R., MIRANDA, A. I. P., AND OLIVEIRA, P. J. Numerical and analytical modeling of unsteady viscoelastic flows: The start-up and pulsating test case problems. *J. Non-Newtonian Fluid Mech. 154* (2008), 153–169.

[10] EYTAN, O., AND ELAD., D. Analysis of intra-uterine fluid motion induced by uterine contractions. *Bull. Math. Biol. 61* (1999), 221.

[11] FAUCI, L. Peristaltic pumping of solid particles. *Comput. Fluids 21* (1992), 583.
[12] GROVE, R. R., AND CHRISPELL, J. *Immersed Boundary Modeling of Journal Bearings in a Viscoelastic Fluid*. PhD thesis, Indiana University OF Pennsylvania, 2013.
[13] JOSEPH, D. D. *Fluid Dynamics of Viscoelastic Liquids*. Springer-Verlag, New York, 1990.
[14] LARSON, R. G. *The Structure and Rheology of Complex Fluids*. Oxford University Press, Oxford, 1998.
[15] LI, M., AND BRASSEUR., J. Non-steady peristaltic transport in finite-length tubes. *J. Fluid Mech. 248* (1993), 129151.
[16] OLDROYD, J. On the formulation of rheological equations of state. *Proceedings of the Royal Society of London. Series A. Mathematical and Physical Sciences 200*, 1063 (1950), 523–541.
[17] PESKIN, C. S. The immersed boundary method. *Acta Numer. 11* (2002), 479–517.
[18] TERAN, J., FAUCI, L., AND SHELLEY, M. Peristaltic pumping and irreversibility of a stokesian viscoelastic fluid. *Phys. Fluids 20* (2008), 73–101.
[19] TERAN, J., FAUCI, L., AND SHELLEY, M. Viscoelastic fluid response can increase the speed and efficiency of a free swimmer. *Phys. Rev. Lett. 104*, 3 (2010), 038101.
[20] VILLONE, M., DAVINO, G., HULSEN, M., GRECO, F., AND MAFFETTONE, P. Particle motion in square channel flow of a viscoelastic liquid: Migration vs. secondary flows. *J. Non-Newtonian Fluid Mech. 195*, (2013), 1 – 8.
[21] WATERS, N. D., AND KING, M. J. Unsteady flow of an elastico-viscous liquid. *Rheol. Acta 9* (1970), 345–355.
[22] WHITE, F. M. *Fluid Mechanics*. McGraw-Hill, 1999.
[23] WRÓBEL, J. K., CORTEZ, R., AND FAUCI, L. Modeling viscoelastic networks in stokes flow. *Phys. Fluids 26*, 11 (2014).
[24] WRÓBEL, J. K., LYNCH, S., BARRETT, A., FAUCI, L., AND CORTEZ, R. Enhanced flagellar swimming through a compliant viscoelastic network in stokes flow. *J. Fluid Mech. 792*, 4 (2016), 775–797.